Hydrodynamics and survivability during post-main-sequence planetary engulfment

RICARDO YARZA , NAELA B. RAZO-LÓPEZ, ARIADNA MURGUIA-BERTHIER, ROSA WALLACE EVERSON, ANDREA ANTONI, MORGAN MACLEOD, MELINDA SOARES-FURTADO, SOARES-FURTADO, ANDREA ANTONI, A

¹Department of Astronomy and Astrophysics, University of California, Santa Cruz, CA 95064, USA

²Center for Interdisciplinary Exploration and Research in Astrophysics (CIERA), 1800 Sherman Ave., Evanston, IL 60201, USA

³Department of Astronomy, University of California, Berkeley, CA 94720, USA

⁴Center for Astrophysics, Harvard & Smithsonian, 60 Garden Street, Cambridge, MA 02138, USA

⁵Department of Astronomy, University of Wisconsin-Madison, 475 N. Charter St., Madison, WI 53703, USA

⁶Department of Applied Mathematics and Statistics, University of California, Santa Cruz, CA 95064, USA

ABSTRACT

The engulfment of substellar bodies (SBs) such as brown dwarfs and planets has been invoked as a possible explanation for the presence of SBs orbiting subdwarfs and white dwarfs, rapidly rotating giants, and lithium-rich giants. We perform three-dimensional hydrodynamical simulations of the flow in the vicinity of an SB engulfed in a stellar envelope. We model the SB as a rigid body with a reflective boundary because it cannot accrete. This reflective boundary changes the flow morphology to resemble that of engulfed compact objects with outflows. We measure the drag coefficients for the ram pressure and gravitational drag forces acting on the SB, and use them to integrate its trajectory during engulfment. We find that SB engulfment can increase the stellar luminosity of a $1M_{\odot}$ star by up to a few orders of magnitude for timescales of up to a few thousand years when the star is $\approx 10R_{\odot}$ and up to a few decades at the tip of the red giant branch. We find that no SBs can eject the envelope of a $1M_{\odot}$ star before it evolves to $\approx 10R_{\odot}$. In contrast, SBs as small as $\approx 10M_{\rm Jup}$ can eject the envelope at the tip of the red giant branch, shrinking their orbits by several orders of magnitude in the process. The numerical framework we introduce here can be used to study the dynamics of planetary engulfment in a simplified setting that captures the physics of the flow at the scale of the SB.

1. INTRODUCTION

Common-envelope evolution (hereafter CEE; Paczynski 1976) is a process in which the expanding envelope of a post-main-sequence star fills its Roche lobe and engulfs a companion (substellar or otherwise). The known census of planetary system architectures implies that a large fraction of planets and brown dwarfs (hereafter substellar bodies, SBs) in main-sequence systems will eventually undergo CEE (Villaver & Livio 2009; Mustill & Villaver 2012; Nordhaus & Spiegel 2013; Schlaufman & Winn 2013; Sun et al. 2018). The CEE phase often results disassociation of the SB companion, which is caused by tidal disruption, ram pressure stripping, and ablation. Throughout this work we will use "planetary engulfment" to refer to common-envelope evolution between and evolved star and an SB, and CEE for the more general interaction of an evolved star with an object of any mass.

SB engulfment stands as a possible explanation to some unsolved problems in stellar and planetary system evolution

Corresponding author: Ricardo Yarza ryarza@ucsc.edu

which have arisen from several types of observations. Firstly, recent observations have identified planets and brown dwarfs closely orbiting subdwarfs and white dwarfs (Schmidt et al. 2005; Littlefair et al. 2006; Maxted et al. 2006; Littlefair et al. 2007; Silvestri et al. 2007; Littlefair et al. 2008; Geier et al. 2009; Charpinet et al. 2011; Breedt et al. 2012; Casewell et al. 2012; Liu et al. 2012; Rebassa-Mansergas et al. 2012; Beuermann et al. 2013; Steele et al. 2013; McAllister et al. 2015; Almeida et al. 2017; Schaffenroth et al. 2015; Parsons et al. 2017; Pala et al. 2018; Casewell et al. 2020; Vanderburg et al. 2020; Schaffenroth et al. 2021; van Roestel et al. 2021, for a summary see Kruckow et al. 2021). These systems might have reached their current orbital configurations dynamically through the Kozai-Lidov mechanism (Kozai 1962; Fabrycky & Tremaine 2007; Katz et al. 2011; Naoz et al. 2012; Socrates et al. 2012; Shappee & Thompson 2013) or via an SB engulfment stage that did not fully disassociate the companion. Engulfment would shrink the system's orbit significantly as a result of orbital energy dissipation through drag forces and tides. In the case of large SBs, it has been suggested that the orbital energy dissipated might be enough to eject the stellar envelope (Nelemans & Tauris 1998; Livio & Soker 1984). Even if the SB does not survive, engulfment might result in an

^{*} NASA Hubble Fellow

[†] NSF Graduate Research Fellow

YARZA ET AL.

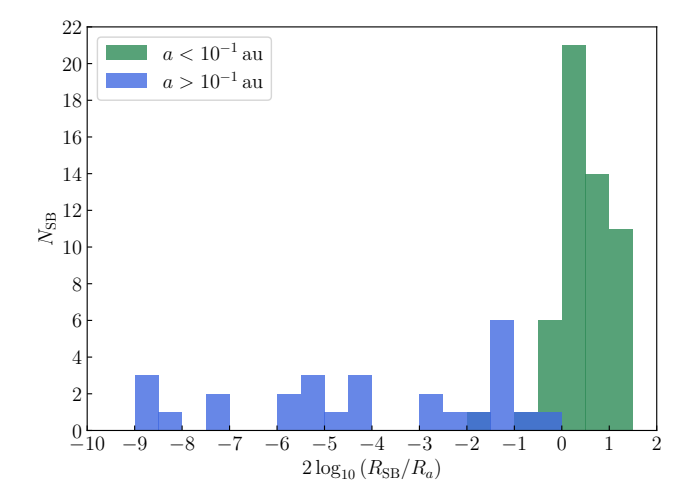


Figure 1. Distribution of exoplanets over the ratio of their geometrical and gravitational cross sections at the onset of engulfment, assuming they are engulfed at their current separations. We include only planets with masses greater than $5M_{\rm Jup}$, as less massive planets are unlikely to survive engulfment (e.g., Nelemans & Tauris 1998; Aguilera-Gómez et al. 2016a). The ratio at the onset of engulfment is predominantly determined by the orbital separation at that time, as this value determines the orbital speed. Data obtained from the NASA Exoplanet Archive (2022).

isolated white dwarf with \gtrsim MG magnetic fields (Nordhaus et al. 2011; Guidarelli et al. 2019).

Additionally, substellar engulfment could explain observations of anomalous rotation among some giant stars. During engulfment, the SB transfers the angular momentum of its orbit into the stellar envelope, resulting in either enhanced or reduced rotation, depending on the alignment of the angular momentum vectors of the star and the orbit. Previous studies (Peterson et al. 1983; Soker 1998; Siess & Livio 1999; Zhang & Penev 2014; Privitera et al. 2016a,b; Qureshi et al. 2018; Stephan et al. 2020) have shown that SB engulfment can speed the surface of giant stars up to the observed speeds, and even up to a significant fraction of their critical speeds.

Similarly, while the stellar surface abundance of ⁷Li generally decreases throughout stellar evolution (Bodenheimer 1965; Deliyannis et al. 2000; Piau & Turck-Chièze 2002; Baumann et al. 2010; Monroe et al. 2013; Meléndez et al. 2014; Carlos et al. 2016, 2019; Soares-Furtado et al. 2020), dropping significantly at the onset of the first dredge-up phase, observations have shown that $\approx 1\%$ of giants are ⁷Li-rich with abundances $\geq 1.5 \,\mathrm{dex}$ (e.g., Wallerstein & Sneden 1982; Brown et al. 1989; Balachandran et al. 2000; Charbonnel & Balachandran 2000; Reddy & Lambert 2005; Carlberg et al. 2010; Charbonnel & Lagarde 2010; Kumar et al. 2011; Martell & Shetrone 2013; Adamów et al. 2014, 2015; Yan et al. 2018; Li et al. 2018; Deepak & Reddy 2019; Gao et al. 2019; Singh et al. 2019). Moreover, $\approx 6\%$ of ⁷Li-rich giants exceed meteoritic abundance strengths of 3.3 dex, indicating that additional ⁷Li must have been generated or deposited within the evolving star (e.g., Balachandran et al. 2000; Zhou

et al. 2019; Singh et al. 2019). The engulfment of SBs, among other processes, has been proposed as an explanation for high surface ⁷Li abundances (e.g., Sandquist et al. 1998; Siess & Livio 1999; Sandquist et al. 2002; Aguilera-Gómez et al. 2016a,b; Soares-Furtado et al. 2020), as SBs do not reach the requisite temperatures to burn their primordial ⁷Li. However, there are other pathways for lithium enrichment, such as self-enrichment through the Cameron-Fowler mechanism (Cameron & Fowler 1971), that act after the early red giant branch (RGB). The existence of these different pathways makes it harder to identify the source of enrichment for stars after the early RGB. Infrared excess is a potential indicator of stellar mass loss from engulfment, and evolved stars with infrared excess also tend to have increased ⁷Li and rotation rates (Mallick et al. 2022).

Several analytical studies (e.g., Metzger et al. 2012; Yamazaki et al. 2017; Jia & Spruit 2018) have focused on SB engulfment among main sequence (MS) stars, where envelope ejection is unlikely because of the high gravitational binding energy. As for post-MS SB engulfment, early analytical estimates (Nelemans & Tauris 1998; Livio & Soker 1984) demonstrated that SBs with masses $^1 \lesssim 10 M_{\rm Jup}$ cannot unbind the envelope of a giant star before being fully destroyed. Staff et al. (2016) performed 3D hydrodynamical simulations of the engulfment of a massive planet by stars in the RGB and AGB, however, their results regarding envelope ejection were limited by numerical resolution. Overall, SB engulfment remains a relatively unexplored problem in the context of hydrodynamical simulations.

Previous work on common-envelope evolution has used the "wind tunnel" numerical formalism to study the flow in the vicinity of the engulfed object, and to account for the effect of density gradients in the stellar envelope (MacLeod & Ramirez-Ruiz 2015a,b; MacLeod et al. 2017; Murguia-Berthier et al. 2017; De et al. 2020; Everson et al. 2020). These density gradients change the flow morphology and give angular momentum to the gravitationally focused gas, thereby changing the forces the embedded object experiences. However, most of this previous work has focused on interactions between an evolved star and a compact companion, for which gravitational drag dominates. For less compact companions, such as planets, the ram pressure drag force might dominate, depending on stellar structure and the dynamics of the companion. While some studies have recognized the importance of ram pressure (Staff et al. 2016; Jia & Spruit 2018), it has not yet been accounted for in detail.

The details of the drag forces experienced by an SB during engulfment will affect the dynamics of the inspiral, the observational signatures associated with it, and ultimately whether the SB can survive engulfment. In this work we study SB engulfment using the wind tunnel numerical formalism, in which we model the flow near the engulfed SB to understand the flow morphology and compute the drag forces. This approach

We use the International Astronomical Union nominal values for solar system constants (Prša et al. 2016).

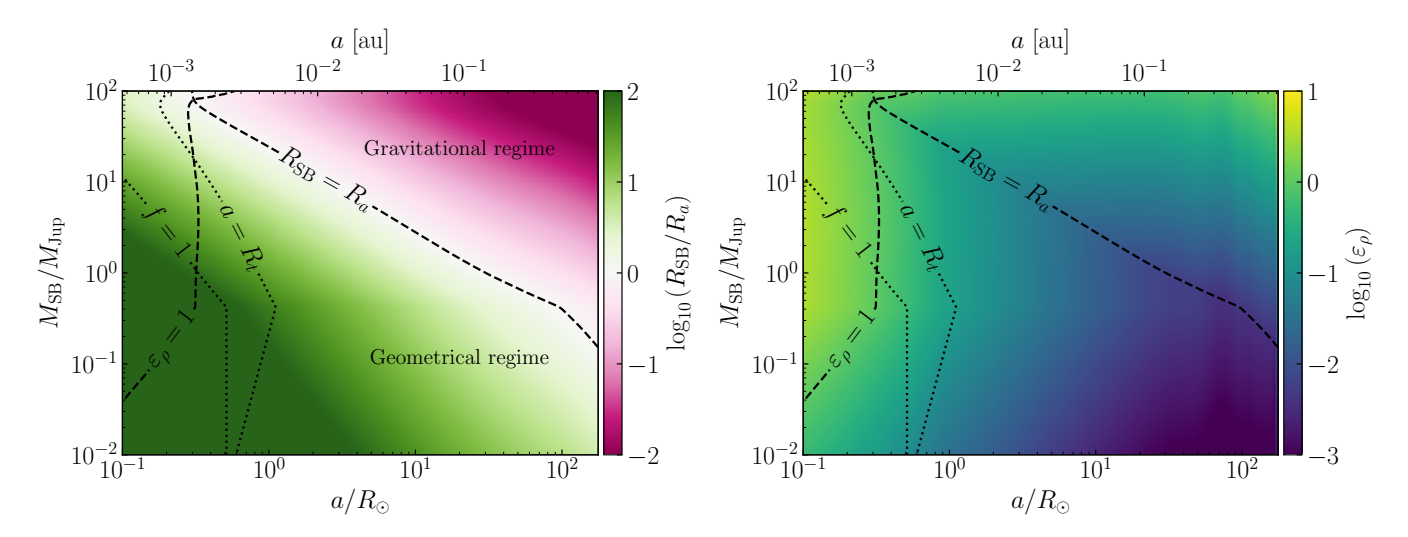


Figure 2. Values for important flow parameters (left: ratio between geometrical and gravitational radii, right: number of density scale heights across the larger radii) as a function of substellar body (SB) mass and position inside a model of the Sun at the tip of the red giant branch. Dashed lines show the transition between geometrical and gravitational regimes, and between mild and strong density gradients. Dotted lines show estimates for SB disruption, either by tidal forces (when the separation equals the tidal radius R_t) or by ram pressure (f = 1, as in equation 3).

allows for approximate inexpensive integrations of the orbit of the SB within the envelope, thereby enabling population studies.

In Section 2, we discuss the physical processes relevant to engulfment, particularly the relative importance of ram pressure and gravitational drag forces. In Section 3, we provide a brief summary of the wind tunnel formalism, our method of computing ram pressure and gravitational drag forces, and our semianalytical inspiral integration. We discuss our results regarding flow morphology, drag coefficients, and potential observational signatures in Section 4. Lastly, Section 6 lists our conclusions.

2. PHYSICAL ASPECTS OF ENGULFMENT

2.1. Gravitational and geometrical regimes

The interactions of the inspiraling SB with the gas in its vicinity are hydrodynamical (ram pressure drag on the geometrical surface of the SB) and gravitational (gravitational drag). Gravitational drag arises from gravitational focusing of material behind the SB as it moves through the gas, resulting in a force against the direction of motion (Ostriker 1999). This force is traditionally described by the formalism of Hoyle & Lyttleton (1939), Bondi & Hoyle (1944), and Bondi (1952). In this formalism, the SB with mass $M_{\rm SB}$ travels relative to the surrounding gas at a speed $v_{\rm orb}$. Gas with an impact parameter smaller than the gravitational radius of the SB, $R_a = 2GM_{\rm SB}/v_{\rm orb}^2$, will be gravitationally focused behind the SB and exert a force $F_g = \pi C_g R_a^2 \rho v_{\rm orb}^2$, where G is the gravitational constant (we use the value given in Tiesinga et al. 2021), ρ is the envelope mass density in its vicinity, and C_q is a dimensionless coefficient of order unity. On the other hand, the pressure field at the surface of the SB will exert a ram pressure force of the form $F_p = \pi C_p R_{\rm SB}^2 \rho v_{\rm orb}^2$.

Estimating the relative importance of gravitational and ram pressure forces is made easier by their similar mathematical form, which represents the momentum per unit time flowing through the cross section for the corresponding interaction. The ratio between ram pressure and gravitational forces is therefore given by the ratio of the cross sections, $(R_{\rm SB}/R_a)^2$, or equivalently the ratio $(v_{\rm orb}/v_{\rm esc,SB})^2$, where $v_{\rm esc,SB} = \sqrt{GM_{\rm SB}/R_{\rm SB}}$ is the escape velocity from the SB.

Previous work on common-envelope evolution has dealt almost exclusively with the engulfment of a compact object, such as a neutron star or black hole, by a giant star, in which case the inspiral of the engulfed object occurs in the gravitational regime. Figure 1 shows the ratio between geometrical and gravitational cross sections at the onset of engulfment for known exoplanets, assuming they are engulfed at their current orbital separations. Planets are likely to be engulfed at separations smaller than their current separations as a result of tidal decay. Since the Keplerian speed is greater at smaller separations, the gravitational radii of planets is likely to be smaller at engulfment than it is today, and more planets will be in the geometrical regime at the onset of engulfment. Equivalently, planets engulfed at earlier stages of stellar evolution are more likely to be in the geometrical regime, as they must orbit their host star more closely in order to be engulfed during earlier stages.

Figure 2 shows the same ratio as Figure 1, but as a function of SB mass and position inside a $\rm M_{\odot}$ star at the tip of the RGB. We computed the properties of this star using the Modules for Experiments in Stellar Astrophysics (MESA, Paxton et al. 2011). As the SB dives deeper into the envelope, its interactions with the gas become increasingly geometrical because the Keplerian speed increases inwards. While it is possible for the Keplerian speed to decrease inwards if the enclosed mass profile is sufficiently steep, the extended post-MS envelopes we consider here do not satisfy this condition. Therefore, SBs gradually transition from the gravitational to the geometrical regime during inspiral.

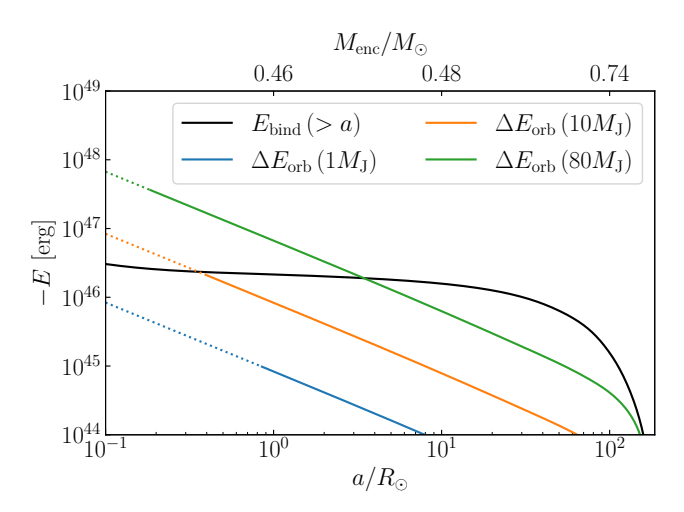


Figure 3. Comparison between the binding energy of exterior material $E_{\rm bind}$ and orbital energy $\Delta E_{\rm orb}$ deposited by substellar bodies (SBs) of different masses, as a function of position inside a model of the sun at the tip of the red giant branch. Orbital energy deposition lines turn dashed at the estimated destruction point for each SB. Assuming an efficiency of 1 for the transfer of orbital energy to the envelope, only SBs with masses $\gtrsim 10 M_{\rm Jup}$ can eject the envelope. For efficiencies $\lesssim 0.1$, only massive brown dwarfs can do so.

As shown in Figure 2, more massive SBs tend to be deeper in the gravitational regime. Between $1M_{\rm Jup}$ and $100M_{\rm Jup}$, SB radius varies only between $0.9R_{\rm Jup}$ and $1.2R_{\rm Jup}$ (Chabrier et al. 2009), almost always sublinearly in $M_{\rm SB}$. Therefore, changes in $R_{\rm SB}/R_a$ for SBs of different masses are approximately a result of changes in $M_{\rm SB}$ only.

The right panel in Figure 2 shows the number of density scale heights $H_{\rho} \equiv \rho/\left(d\rho/dr\right)$ across the SB,

$$\varepsilon_{\rho} \equiv \max\left(R_{\rm SB}, R_a\right) / H_{\rho},$$
(1)

which quantifies the importance of density gradients to the flow at the scale of the SB. This panel shows that engulfed SBs typically experience mild ($0 \le \varepsilon_\rho \lesssim 1$) density gradients. This Figure determines the parameter space that we must sample in our hydrodynamical simulations to ensure we capture the flow morphology near the SB throughout engulfment.

2.2. Destruction of the substellar body

We consider two criteria for where in the envelope the SB will be destroyed. Firstly, we estimate the SB will be tidally disrupted when

$$\frac{\langle \rho_{\rm enc} \rangle}{\langle \rho_{\rm SB} \rangle} = 1,\tag{2}$$

where $\langle \rho_{\rm enc} \rangle$ is the average density of the material enclosed by the SB's orbit, and $\langle \rho_{\rm SB} \rangle$ is the average density of the SB. We estimate the SB will be disrupted by ram pressure when (Jia & Spruit 2018)

$$f \equiv \frac{\rho v_{\text{orb}}^2}{\langle \rho_{\text{SB}} \rangle v_{\text{esc.SB}}^2} = 1.$$
 (3)

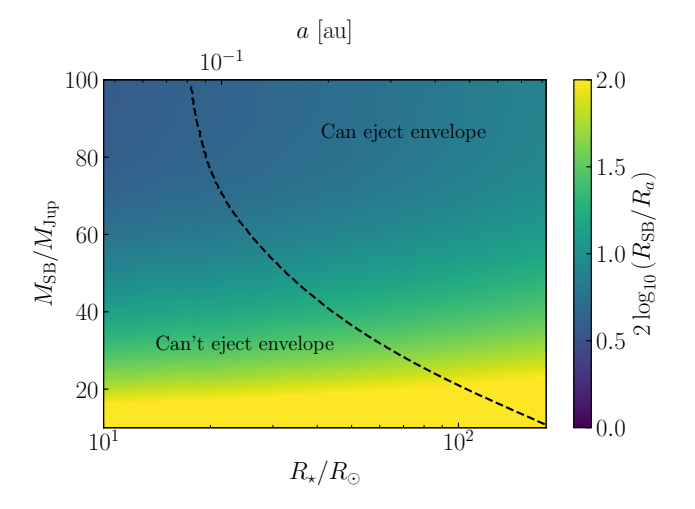


Figure 4. Ratio of geometrical and gravitational cross sections at the point of envelope ejection or SB (or low-mass star, for masses $\gtrsim 80 M_{\text{Jup}}$) tidal disruption, as a function of stellar radius over time and SB mass. The dashed line shows the minimum mass required to eject the envelope. When engulfment ends, either by destruction of the SB or envelope ejection, all SBs are in the geometrical regime.

Figure 2 also shows that all SBs considered here will be in the geometrical regime before being destroyed.

2.3. Envelope ejection

To estimate analytically whether envelope ejection is possible, we use the α formalism (Webbink 1984), which states that an embedded object will be able to eject material exterior to the orbital separation a if the binding energy of that material is smaller in magnitude than the change in orbital energy of the SB, i.e. $\alpha |\Delta E_{\rm orb}| > |E_{\rm bind}(>a)|$, where

$$\Delta E_{\rm orb} = -\frac{GM_{\rm enc}M_{\rm SB}}{2a} + \frac{GM_{\star}M_{\rm SB}}{2R_{\star}},\tag{4}$$

$$E_{\text{bind}}(>a) = -4\pi G \int_{-\pi}^{R_{\star}} M_{\text{enc}} \rho a' \, da', \tag{5}$$

 $\alpha \leq 1$ is the efficiency of energy deposition into the envelope, and $M_{\rm enc}$ is the enclosed mass at orbital separation a. Figure 3 shows $E_{\rm bind}$ for a MESA model of the Sun at the tip of the RGB, as well as ΔE_{orb} for SBs of several masses. According to the α formalism, objects with masses $\gtrsim 10 M_{\rm Jup}$ will be able to eject the envelope of this model before being destroyed. Figure 4 shows R_{SB}/R_a at the point in the stellar envelope where the SB is either destroyed or ejects the envelope, as a function of SB mass and stellar radius (equivalently, time). The dotted line shows the minimum SB mass to eject 90% of the envelope mass before being destroyed, according to the α formalism. We define the core-envelope boundary as the radial coordinate at which the hydrogen mass fraction increases above 1/10. Since the star becomes more extended as it ascends the RGB, its binding energy decreases and it becomes easier for smaller SBs to eject the envelope. No SB with mass $< 100 M_{\rm Jup}$ can eject the envelope of an ${\rm M}_{\odot}$

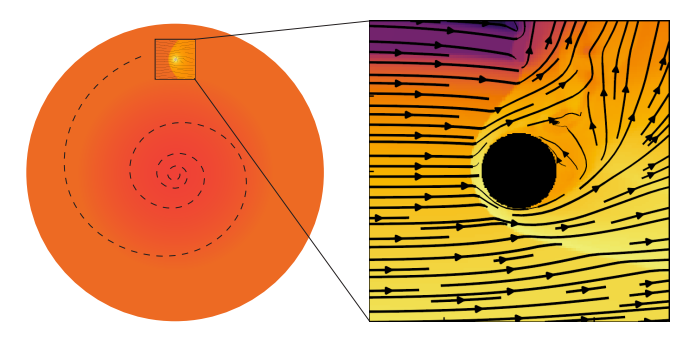


Figure 5. Schematic of the wind tunnel numerical setup. Left: substellar body (SB) embedded in the envelope of a giant star, with an inspiral trajectory shown as a dashed line. Right: density slice and velocity streamlines in a wind tunnel simulation of the embedded object. The orbital speed is higher than the local sound speed, so the object will drive a shock as it moves through the stellar envelope.

star early in the RGB. All SBs are in the geometrical regime when they are destroyed or when they eject the envelope, highlighting the need for numerical models that account for the ram pressure drag force, especially in the late stages of the inspiral.

3. NUMERICAL METHODS

3.1. Wind tunnel hydrodynamical simulations

Global simulations of SB engulfment that account for changes in the internal structure of the post-MS star and the SB are computationally unfeasible because the scale of the flow in the vicinity of the SB is $\approx \max(R_{SB}, R_a) \approx R_{Jup}$, while the scale of the inspiral and the star is $\approx 1\,\mathrm{au}\,\approx$ $10^3 R_{\text{Jup}}$. This disparity of scales motivates an approach that isolates the processes occurring at each scale, not only for computational feasibility and accuracy, but also for understanding the role of each of these processes and eventually the interplay between the processes at different scales. Here we perform simulations of the flow within a few max (R_{SB}, R_a) of the SB, which we model as a rigid object. Our objective is to understand the morphology of the flow in the vicinity of the SB, and the forces acting on the SB. Quantitative measurements of these forces will allow us to perform approximate numerical integration of the inspiral trajectory. This approach allows inexpensive yet reasonably accurate exploration of a much larger region of parameter space, which makes it useful for population synthesis models that statistically constrain planetary formation.

We use the "wind tunnel" numerical setup introduced in (MacLeod et al. 2017), and illustrated in Figure 5. We simulate a local domain in the frame of the engulfed SB, and we supply a time-independent and spatially uniform "wind" from the $-\hat{x}$ direction. The initial conditions are determined by the set of parameters ε_{ρ} , q, $R_{\rm SB}/R_a$, and the density at y=0. We set this density to $1~{\rm g~cm^{-3}}$ for simplicity, although this value does not change the morphology of the flow and therefore the drag coefficients. Hydrostatic equilibrium in the envelope

relates $arepsilon_{
ho}$ and q to the upstream Mach number ${\cal M}$ as

$$\varepsilon_{\rho} = \frac{2q}{\left(1+q\right)^2} \mathcal{M}^2. \tag{6}$$

We set the wind speed to $1~{\rm cm~s^{-1}}$ (for the same reasons as the density), and set the pressure at y=0 so that the flow has the Mach number implied by hydrostatic equilibrium, ε_{ρ} , q, and the wind speed. Once the flow properties are computed at y=0, we integrate the equations of hydrostatic equilibrium for a massless atmosphere up to the boundaries in the $\pm \hat{y}$ directions. In the $-\hat{y}$ direction, we extend hydrostatic equilibrium to the ghost zones. We add the gravitational field of the enclosed stellar mass so that the gas remains in hydrostatic equilibrium in the absence of external forces. The external force in our simulations, leading to the deflection of the gas, is the gravity of the SB. For all other boundaries, we use outflow boundary conditions, in which gas is allowed to leave the domain but not enter it. For more details, see MacLeod et al. (2017). The numerical setup is available online (see Appendix B).

This numerical setup is written for the FLASH (Fryxell et al. 2000; Dubey et al. 2014, 2015) multiphysics code. The setup uses FLASH to solve the equations of inviscid hydrodynamics on a Cartesian mesh with adaptive mesh refinement. We use an ideal gas equation of state $P=(\gamma-1)\,u$, where P is the pressure, γ the ratio of specific heats (which we take to be 5/3), and u is the internal energy per unit volume. We set the minimum and maximum cell sizes to $R_a/1024$ and $R_a/8$, respectively, and refine based on internal energy and the rigid boundary. See Appendix A.1 for hydrodynamics convergence tests

These simulations neglect the curvature of the velocity field within the domain. Equivalently, we approximate the direction of the azimuthal unit vector as constant within the domain. This assumption is valid as long as the radius of curvature of the velocity field is much larger than the length of the box along the direction of orbital motion. Since the motion is assumed circular, the radius of curvature is the radial coordinate, which for most of the inspiral is of order the radius of the star R_{\star} . The size of the domain is $\sim\!\!R_{\rm SB}$ so, since $R_{\rm SB}\ll R_{\star}$, curvature can be neglected.

The initial conditions in our simulations place the SB in a circular Keplerian orbit inside the stellar envelope. The actual orbital evolution before engulfment is dictated by tides and mass loss (Villaver & Livio 2007, 2009; Nordhaus & Spiegel 2013; Sun et al. 2018; MacLeod & Loeb 2020). While SB orbits tend to circularize during the MS and post-MS (Villaver et al. 2014) as a result of tides, there is observational evidence of SBs with nonzero eccentricities in close orbits around evolved stars (Grunblatt et al. 2018, 2022). SBs are significantly denser than the giant stars we consider, so they will undergo Roche lobe overflow only near the stellar core (Metzger et al. 2012).

3.2. Reflective inner boundary condition

Previous simulations of common-envelope evolution between extended stars and compact objects have modeled the

compact object as a numerical "sink" inside of which fluid variables are multiplied by a small number, creating a vacuum that allows the object to accrete the surrounding material. Physically, these objects are able to accrete because the flow accumulating around them reaches the conditions required to cool via neutrino emission (MacLeod & Ramirez-Ruiz 2015a; Fragos et al. 2019).

On the other hand, there is no such cooling channel for gas accumulated at the surface of the SB at these high accretion rates. Due to the large optical depth photons are unable to escape and, so the gas is unable to cool. The timescale over which radiation will carry energy through the optically thick surrounding material, allowing it to be accreted, is much longer than the inspiral timescale.

We therefore model the surface of the SB using a reflective boundary. We use FLASH's unsplit hydrodynamics solver, which is the hydrodynamics version of the unsplit magneto-hydrodynamics solver (Lee 2013). The reflective boundary condition is applied at the surface of the stationary rigid body, i.e. in the rigid body cells adjacent to the fluid cells. With the reflective condition, numerical stability requires a CFL ≤ 0.3 because of the reduced reconstruction order near the boundary.

During the engulfment of a compact object by a giant star, the geometrical size of the object is negligible ($R_{\rm SB} \ll R_a$), whereas an engulfed SB can have $R_{\rm SB} \gtrsim R_a$. Previous simulations (e.g., Figure 10 in Ruffert & Arnett 1994) have shown that when the radius of the "sink" object is $\gtrsim 0.2R_a$, the shock morphology changes into a "tail shock" that trails the path of the object. As we will see (Figure 6), the reflective boundary prevents this change in morphology. These qualitative differences highlight the importance of using a reflective boundary for SBs in capturing the flow morphology and computing accurate drag coefficients.

Since we use Cartesian coordinates, the surface area elements point in the directions of the Cartesian axes instead of radially outward, which qualitatively affects some of its properties even at high resolution (see Section 3.3).

3.3. Drag force measurements

We measure the forces on the object once the simulation reaches steady state, which takes a few $\max\left(R_a,R_{\mathrm{SB}}\right)/v_{\mathrm{orb}}.$ We measure the gravitational drag force as in MacLeod et al. (2017), integrating the gravitational force of the surrounding density field up until $1.6R_a.$ In steady state, we compute the ram pressure drag force as

$$\mathbf{F}_{p} = -\oint_{S} P \, d\mathbf{A},\tag{7}$$

where S if the surface of the SB. We neglect the tangential stresses that arise from the viscosity of the fluid. We use FLASH to solve the equations of inviscid hydrodynamics; while there is some numerical viscosity as a result of the discretization of the equations, solving the inviscid equations means the simulations do not have a boundary layer around the SB, which can potentially affect the ram pressure drag

and the viscous stresses acting on it. For the same reason we do not study the dependence of the ram pressure drag on the Reynolds number. However, as shown in Figure 7, our simulations reproduce the standard value for the drag coefficient of a smooth sphere.

Computing the ram pressure drag force by summing the product of the pressure at fluid cells adjacent to the rigid boundary multiplied and the area element of that boundary will yield incorrect results. The reason is that as the resolution increases, the volume of the SB converges to $4\pi R_{\rm SB}^3/3$ but the area does not converge to $4\pi R_{\rm SB}^2$. This lack of convergence is a result of the Cartesian discretization of the surface. Instead, we compute the integral by interpolating the pressure on a spherical shell of radius $R_{\rm SB}$ and numerically integrating that function over the shell. We verified the convergence of this method by computing the force exerted on the object by an analytical pressure field.

The coefficients measured from the steady state simulations are valid if the timescale over which the simulation reaches steady state is much shorter than the inspiral timescale. For SBs, whose inspirals take hundreds of years, this condition always holds. Therefore, the flow can be approximated as being in steady state throughout the inspiral.

3.4. Parameter space sampled

We assume that the drag coefficients depend only on parameters that affect the flow morphology, which we in turn assume to be the Mach number \mathcal{M} , ε_{ρ} , and $R_{\rm SB}/R_a$. We compute geometrical and gravitational drag coefficients as described in Section 3.3 on a three-dimensional grid in the domain

$$-3 \le \log_{10} q \le -1,$$
 (8)

$$-1 \le \log_{10} \varepsilon_{\rho} \le 0, \tag{9}$$

$$0.3 \le R_{\rm SB}/R_a \le 1,$$
 (10)

with four logarithmically spaced points along q and ε_{ρ} , and seven along $R_{\rm SB}/R_a$. We chose this domain based on the range of values we expect for these parameters (see Figure 2). We will use the drag coefficients to integrate the trajectory of the SB inside the stellar envelope. The drag coefficients are available online (see Appendix B).

4. SIMULATION RESULTS

4.1. Flow morphology and drag coefficients

Figure 6 shows representative density slices of wind tunnel simulations at different $R_{\rm SB}/R_a$ and ε_ρ , and Figure 7 shows the geometrical and gravitational drag coefficients as a function of the same set of parameters. The mass ratio in this set of simulations is 10^{-2} . At low $R_{\rm SB}/R_a$, gas will accumulate behind the SB as in the Bondi-Hoyle-Lyttleton formalism. However, since the SB cannot accrete, material will accumulate at the boundary and be in approximate hydrostatic equilibrium. The pressure force exerted by this material will oppose the pressure force from material accumulated in front of the object a result of compression when the SB moves

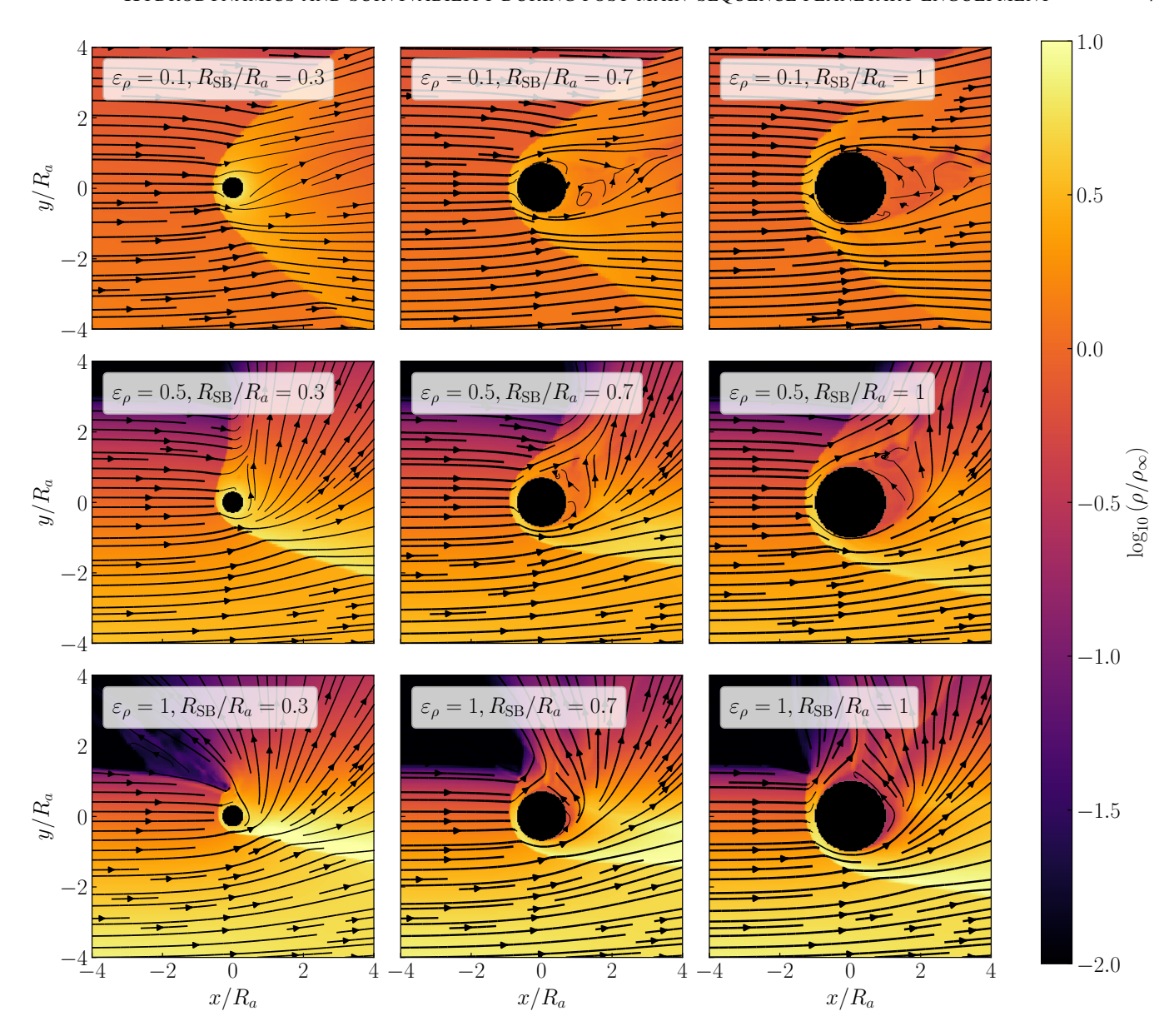


Figure 6. Density (in units of upstream density at y=0, ρ_{∞}) in wind tunnel simulations as a function of space, for several values of the number of density scale heights per gravitational radius (ε_{ρ}), and the ratio between geometrical and gravitational radii $R_{\rm SB}/R_a$. These slices are taken at $t=25R_a/v_{\rm orb}$, where $v_{\rm orb}$ is the upstream gas speed. This figure highlights the transition between the gravitational and geometrical regimes for different density gradients. At low $R_{\rm SB}/R_a$, a spherically symmetric envelope of material that cannot be accreted forms around the SB, suppressing ram pressure drag. At high $R_{\rm SB}/R_a$, a vacuum forms behind the SB, increasing ram pressure drag and suppressing gravitational drag. An animated version of this figure is available in the HTML version of the article. The animation shows the time evolution of the density slices from t=0 to $t=35R_a/v_{\rm orb}$.

through the gas. The combined effect is that a spherically symmetric gas profile in hydrostatic equilibrium will form around the SB, suppressing the ram pressure drag force. This result is consistent with previous simulations in this regime (Thun et al. 2016).

At high $R_{\rm SB}/R_a$, the SB does not exert a gravitational pull strong enough to accumulate material behind it, so this region contains low-density turbulent gas. The lack of material behind the SB means the ram pressure force exerted by gas in

front of the SB is now unopposed, and that the gravitational drag force is greatly reduced.

The dependence of the drag coefficients on the density gradient, the Mach number, and the mass ratio can be understood from the relationship between these parameters in hydrostatic equilibrium (Equation 6), and the flow morphology in Figure 8. Simulations with stronger density gradients have larger drag coefficients because the SB interacts with higher density gas (from deeper in the envelope) both geometrically and

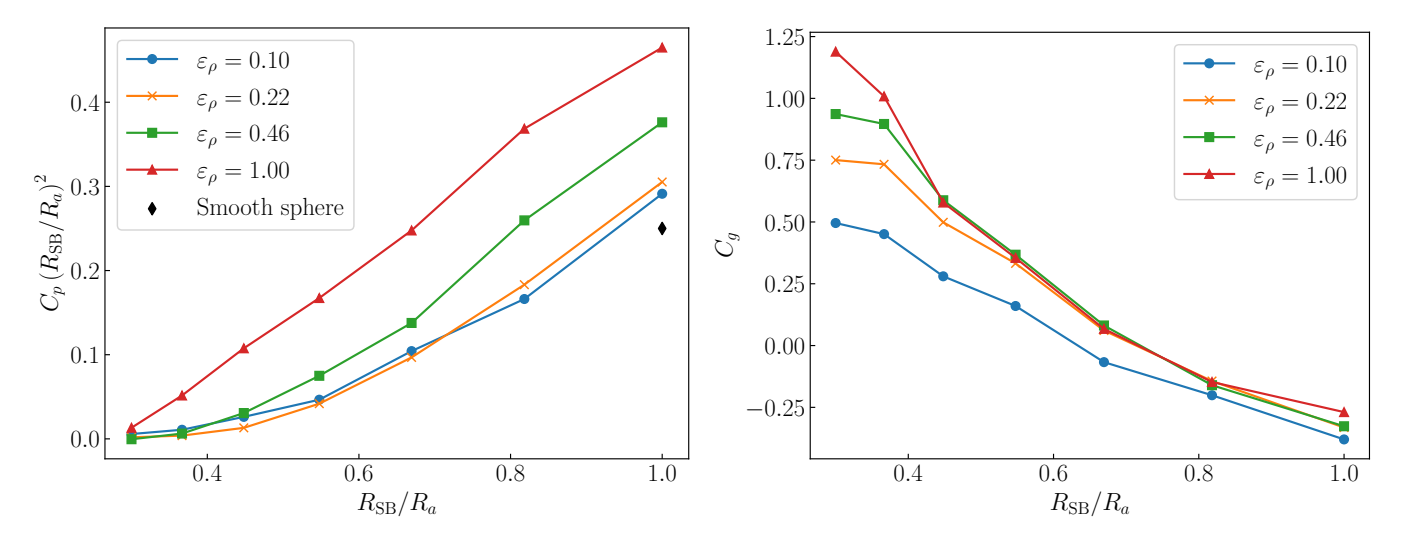


Figure 7. Ram pressure (left) and gravitational (right) drag coefficients for simulations in the parameter space defined by Equations 9 and 10, with $q=2\times 10^{-2}$. We scale the ram pressure drag coefficient by $(R_{\rm SB}/R_a)^2$ to facilitate comparison between the magnitudes of the two forces (see Equation 14). The black triangle shows the ram pressure drag coefficient for a smooth sphere at Reynolds number $\sim 10^4$. This coefficient is typically quoted as 0.5 assuming a drag equation $F=C_p\pi\rho v^2R_{\rm SB}^2/2$, whereas our drag equation absorbs the factor of 1/2 so that geometrical and gravitational drag forces have the same mathematical form. In our form, the standard smooth sphere coefficient is 0.25.

gravitationally. From hydrostatic equilibrium, increasing the mass ratio at a fixed Mach number will result in a stronger density gradient, and larger drag coefficients.

Similarly, at a given density gradient, larger Mach numbers will result in a narrower shock opening angle, allowing focused material to accumulate closer to y=0, increasing the horizontal component of the drag force and therefore the gravitational drag coefficient. Higher Mach numbers also result in increased gas compression in front of the SB, increasing the ram pressure drag coefficient. At fixed density gradient, increasing the Mach number requires decreasing the mass ratio, so increasing mass ratios reduce the drag coefficient.

Some of our simulations in the $R_{\rm SB} \sim R_a$ regime have a negative gravitational drag coefficient, meaning the gravitational drag force acts along the direction of motion of the object, instead of against it. Negative drag coefficients have been found for compact objects with outflows (Gruzinov et al. 2020; Li et al. 2020; Kaaz et al. 2022) and luminous planetesimals moving through a disk (Masset & Velasco Romero 2017; Masset 2017). In these cases, feedback from the object can interfere with the flow at impact parameters R_a that would have been gravitationally focused behind the object in the absence of feedback. Since this gas can no longer be gravitationally focused, an underdensity forms behind the object. In our simulations, the rigidity of the SB and the reflective condition enforced at its surface have this effect when $R_{\rm SB} \sim R_a$. We find negative drag coefficients when the Mach number is low, since the stand-off distance of the shock is larger because the gas is less compressed in front of the object. The acceleration from the gravitational drag will increase the Mach number, reducing the amount of material accumulated in front of the object, making the gravitational drag force less negative. In our simulations (and inspiral trajectories) this

effect is therefore self-regulating, in that it does not lead to indefinite acceleration of the SB.

5. APPLICATIONS TO SUBSTELLAR ENGULFMENT

5.1. Inspiral integration method

The equation of motion for the SB inside the envelope can be written as

$$M_{\rm SB} \frac{d\mathbf{v}}{dt} = (M_{\rm SB} - \rho V_{\rm SB}) \,\mathbf{g} + \mathbf{F}_{\rm drag},\tag{11}$$

where ${\bf v}$ is the velocity of the SB, t is time, $V_{\rm SB}$ is the volume of the SB, and ${\bf g}=-GM_{\rm enc}{\bf \hat r}/r^2$ is the gravitational acceleration as a result of the enclosed mass. The term $\rho V_{\rm SB}{\bf \hat g}$ is the buoyancy acting on the SB, which is important when the local density equals the average density of the SB. Since the local density is always smaller than the average enclosed density, and the SB will be tidally disrupted approximately when the average enclosed density is equal to its own mean density, buoyancy won't be important before the SB is destroyed. We write this equation in 2D polar coordinates as the set

$$\ddot{r} = -\frac{GM_{\text{enc}}}{r^2} \left(1 - \frac{\rho}{\rho_{\text{SB}}} \right) + \frac{v_{\theta}^2}{r} + \frac{\mathbf{F}_{\text{drag}} \cdot \hat{\mathbf{r}}}{M_{\text{SB}}}, \tag{12}$$

$$\ddot{\theta} = -\frac{2\dot{r}\dot{\theta}}{r} + \frac{\mathbf{F}_{\text{drag}} \cdot \hat{\theta}}{rM_{\text{SB}}}.$$
 (13)

Drag forces that oppose the radial motion of the SB are negligible because $\dot{r} \ll r\dot{\theta}$, so we write the drag forces as

$$\mathbf{F}_{\text{drag}} = -\operatorname{sgn}(v_{\theta})\rho v_{\theta}^{2}\sigma_{g} \left[C_{g} + \left(\frac{R_{\text{SB}}}{R_{a}} \right)^{2} C_{p} \right] \hat{\theta}, \quad (14)$$

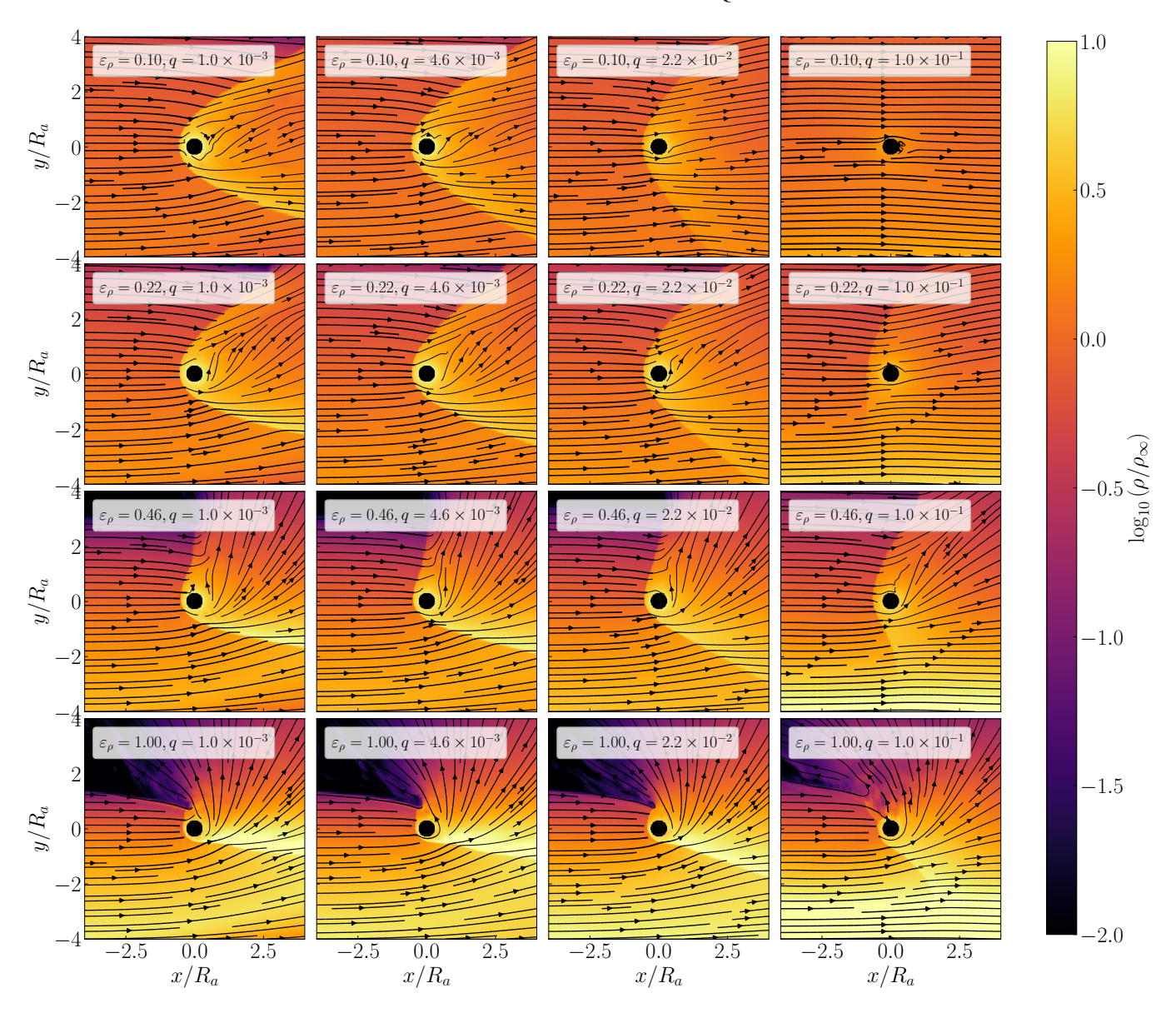


Figure 8. Density (in units of upstream density at y=0, ρ_{∞}) in wind tunnel simulations as a function of space, for several values of the number of density scale heights per gravitational radius (ε_{ρ}), and the ratio between the mass of the substellar object and the mass enclosed by its orbit (q). The ratio between geometrical and gravitational radii is 0.3 in all panels. These slices are taken at $t=25R_a/v_{\rm orb}$, where $v_{\rm orb}$ is the upstream gas speed. Larger density gradients and Mach numbers result in higher drag coefficients. An animated version of this figure is available in the HTML version of the article. The animation shows the time evolution of the density slices from t=0 to $t=30R_a/v_{\rm orb}$.

where sgn is the sign function. We linearly interpolate the dimensionless drag coefficients C_g and C_p based on the results of the hydrodynamical simulations. For points outside the domain of the interpolation, we used the nearest available point. We integrate these equations using the eight-order Runge-Kutta Prince-Dormand method from the GNU Scientific Library (Galassi et al. 2009). This inspiral integration code is available as free software (see Appendix B).

We set the initial conditions for equation 11 to be $r=r_0=0.9R_\star$, $\theta=0$, and Keplerian rotation, i.e. $\dot{r}=0$ and $\dot{\theta}=\sqrt{GM_{\rm enc}/r_0^3}$. At every timestep we interpolate the properties of the stellar profile using the GSL implementation of the

moniticity-preserving Steffen method (Steffen 1990). We halt the integration when $r \leq R_{\rm SB}$, and apply the destruction criteria later during postprocessing.

We compute the profiles we use for integrating the trajectory of the SB using MESA. The timescale for inspiral, as we will see, is $\lesssim 10^4~\rm yr$, while the timescales R/\dot{R} and L/\dot{L} over which radius and luminosity change significantly, respectively, are $\gtrsim 10^6~\rm yr$ in these MESA models throughout the RGB. We therefore assume that stellar structure remains constant throughout engulfment. We do not model the effects of engulfment on stellar structure.

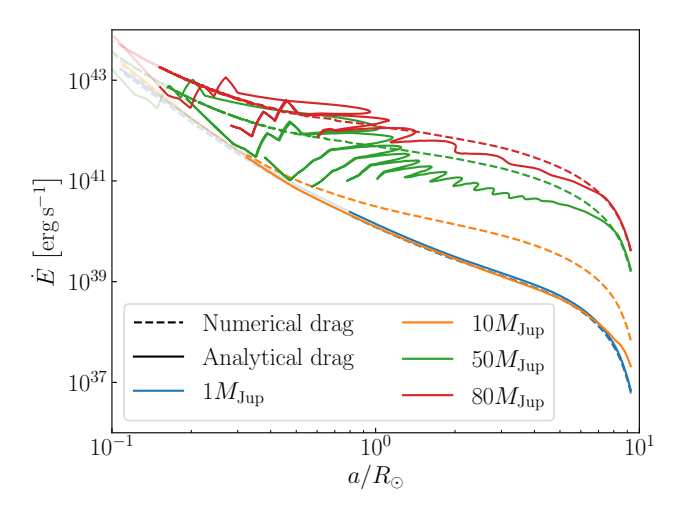


Figure 9. Energy deposition rate as a position of radial coordinate in the envelope of a $1M_{\odot}$ star evolved to $10R_{\odot}$, for inspirals of substellar bodies (SBs) of different masses. Dashed and solid lines correspond to analytical and numerical drag coefficients, respectively. Lines turn transparent at the estimated point of SB destruction. Using the numerical drag coefficients can lead to differences in the energy deposition rate of up to an order of magnitude, depending on the region of parameter space probed.

5.2. Inspiral timescales

The rate of orbital energy dissipation is the work per unit time done by the drag force, so the inspiral time can be estimated analytically for ram pressure drag as

$$\tau_{\rm insp,p} \approx \frac{E_{\rm orb}}{\dot{E}_{\rm orb}} = \frac{GM_{\rm SB}M_{\rm enc}}{2aF_pv_{\rm orb}} = \frac{GM_{\rm enc}M_{\rm SB}}{2\pi C_paR_{\rm SB}^2v_{\rm orb}^3\rho}, \quad (15)$$

and for gravitational drag as

$$\tau_{\rm insp,g} \approx \frac{GM_{\rm SB}M_{\rm enc}}{2aF_gv_{\rm orb}} = \left(\frac{M_{\rm enc}}{M_{\rm SB}}\right) \frac{v_{\rm orb}}{8\pi GC_g a\rho}.$$
(16)

In the geometrical regime, SBs of larger mass decay more slowly because they experience approximately the same force, but have larger inertia. As before, radius is almost constant in mass between $1M_{\rm Jup}$ and $100M_{\rm Jup}$, so the change in the geometrical inspiral timescale as a result of changes in radius is negligible. In the gravitational regime, however, more massive SBs inspiral faster because the gravitational cross section scales as the square of their mass, overcoming the inertial term.

The inspiral timescale is sensitive to the density of the stellar envelope at the onset of engulfment because the object will spend most of its time in the outer envelope, where drag forces are smaller. The initial density will depend on the amount of mass stripped from the star at the end of post-MS orbital evolution. Accordingly, the inspiral timescale is determined by $R_{\rm SB}/R_a$ at the onset of engulfment. For evolved stars, tides might determine the inspiral time by being the dominant force at the onset of engulfment (e.g. Stephan et al. 2020), but we do not account for them here.

We find that all objects engulfed near the tip of the RGB inspiral on a timescale comparable to Equation 16 because the star is extended. In earlier stages of stellar evolution, however, it is possible for less and more massive SBs to inspiral on the timescales given by Equation 15 and Equation 16, respectively. Since these timescales have opposite scaling in mass, intermediate-mass SBs will take the longest to inspiral (see Appendix A).

5.3. Stellar brightening

Energy deposited into the star will result in an adjustment from the star to a new configuration in hydrostatic equilibrium and, on a longer timescale, on radiation of the energy deposited. If an amount of energy dE is deposited into the star, the upper bound (assuming all energy is radiated) for the average increase in stellar luminosity is $dL = dE/\tau_{\rm KH}$, where $\tau_{\rm KH}$ is the energy transport timescale from the location of energy deposition to the surface, as a result of radiative diffusion in the core and convection in the envelope. More generally, if energy is deposited continuously, the time-averaged additional luminosity at time t during the inspiral is

$$\Delta L(t) = \int_{t_0}^{t} \frac{\dot{E}}{\tau_{\text{KH}}} dt', \qquad (17)$$

where we determine t_0 by noticing that energy deposited a time $t-t_0$ ago contributes to the increase in the average luminosity only if $t-t_0 \leq \tau_{\rm KH} \, (t_0)$, since if $t-t_0 > \tau_{\rm KH} \, (t_0)$, the energy deposited at t_0 has already been radiated away. If the energy deposition increases sharply in the inner parts of the inspiral, $\dot{E} \approx \delta \, (t'-t) \, \Delta E \, (t')$ in equation 17, and $\Delta L \approx \Delta E / \tau_{\rm KH}$ (e.g. MacLeod et al. 2018).

We compute \dot{E} as the work per unit time done by the drag forces, i.e.

$$\dot{E} = \mathbf{F}_{\text{drag}} \cdot \mathbf{v}. \tag{18}$$

We compute the energy transport timescale by adding the cell crossing times in the stellar profile, where the crossing time for each cell is determined by the most effective energy transport mechanism at that location (either radiative diffusion or convection).

Figure 9 shows a comparison of the energy deposition rate into the envelope using analytical ($C_g=1,\,C_p=0.25$) and numerical drag coefficients. The energy deposition from the $10M_{\rm Jup}$ SB is drastically reduced in the outer parts of the inspiral when using numerical drag coefficients because they predict lower gravitational drag. The orbits of massive SBs are increasingly eccentric because the gravitational drag coefficient varies significantly over the course of a single orbital period.

Figure 10 shows the quantities involved in our calculation of the average luminosity for the engulfment of SBs of varying masses by a $1M_{\odot}$ star evolved to $10R_{\odot}$. The top left panel compares the inspiral and energy transport timescales as a function of the orbital separation (equivalently, time) during the inspiral. When the inspiral timescale is much longer than the energy transport timescale, the luminosity is close to the energy deposition rate, whereas deep in the envelope

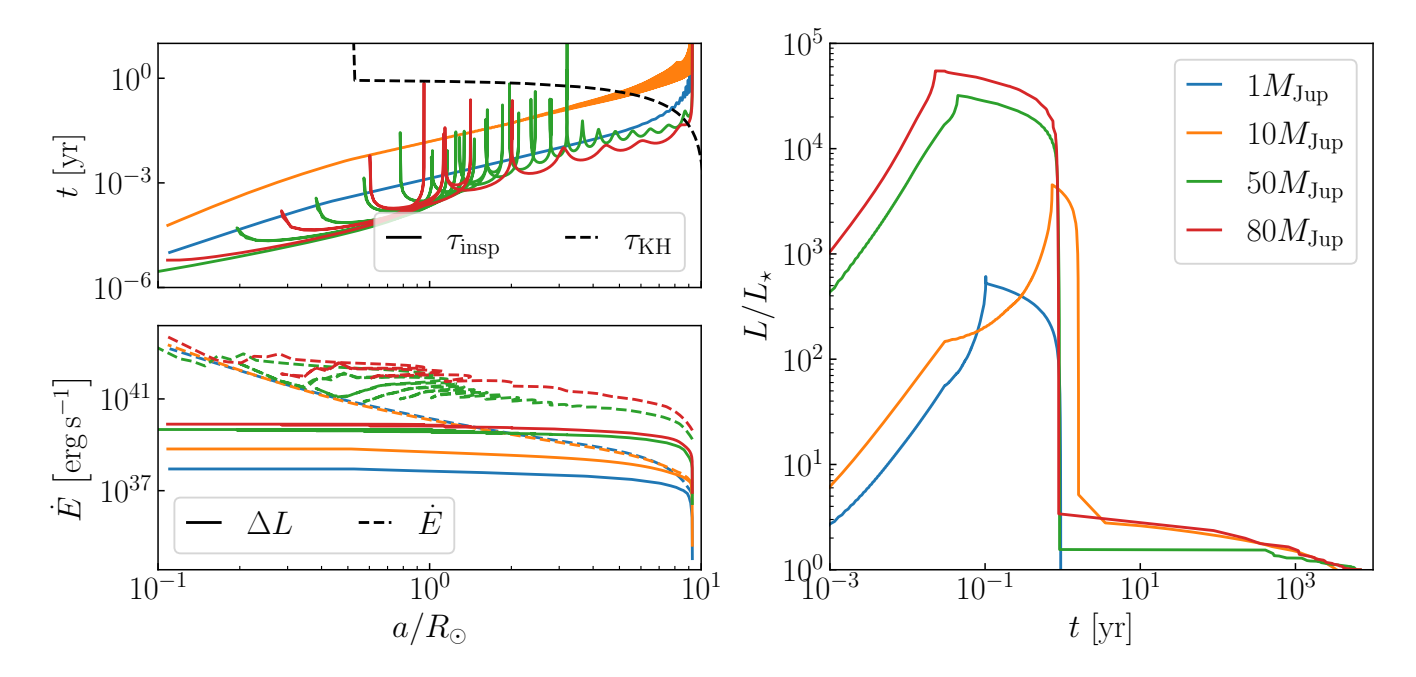


Figure 10. Top left panel: inspiral and Kelvin-Helmholtz timescales as a function of orbital separation a during inspiral. The inspiral timescales for the two more massive substellar bodies show peaks because we define the inspiral timescale as $|a/\dot{a}|$ and as a result of eccentricity in the orbit \dot{a} changes sign at some points during the inspiral, yielding peaks at the smallest values of $|\dot{a}|$. Bottom left panel: luminosity to the energy deposition rate given by the drag forces, again as a function of position inside the profile. When the Kelvin-Helmholtz time is much longer than the inspiral time, the luminosity is much smaller than the energy deposition rate. Right panel: luminosity as a function of time, compared to the unperturbed stellar luminosity.

the energy transport timescale is much longer than the inspiral timescale, making the luminosity much smaller than the energy deposition rate. This behavior is shown in the bottom left panel. The right panel shows the luminosity.

In general, we find that, from $R_\star=10R_\odot$ to the tip of the RGB, the additional luminosity from engulfing SBs of all masses $\gtrsim M_{\rm Jup}$ will be larger than the stellar luminosity, in many cases by several orders of magnitude (see Metzger et al. 2017). When the star has just started ascending the RGB, small SBs are destroyed in the outer layers of the envelope. However, the comparatively high density of the envelope and low luminosity of the star mean that even the inspiral of these small, short-lived SBs will exceed the stellar luminosity. On the other hand, evolved stars will have higher luminosities and lower densities, but SBs can survive deep enough to exceed the stellar luminosity.

After the SB is destroyed, the timescale for the luminosity to return to its original value is roughly the energy transport timescale at the point of destruction. The energy transport timescale becomes shorter as the star ascends the RGB. For a given star, more massive SBs, which tend to also be denser as a result of the mass-radius relation, will result in a longer increase in luminosity because they survive deeper into the envelope. For a model of the Sun evolved to a radius of $10R_{\odot}$, the timescales for increased luminosity range from $\sim 1~\rm yr$ for a $1M_{\rm Jup}$ planet to $\sim 5000~\rm yr$ for a $50M_{\rm Jup}$ brown dwarf, as shown in Figure 10. On the other hand, for a model of the

Sun at the tip of the RGB, the timescales range from \sim 1 yr to \sim 25 yr for the same range of SB masses.

5.4. Engulfment outcomes

The drag coefficients from our hydrodynamical simulations allow us to directly compute the energy deposited into the envelope, which is the total work done by the drag forces, by integrating Equation 18 in time. Figure 11 shows known SBs (NASA Exoplanet Archive 2022) as a function of their mass and present-day orbital separation. The dashed line near the top-right corner shows the minimum SB mass such that the SB deposits enough energy to eject at least 90% of the mass of the envelope. SBs below this line are destroyed without ejecting the envelope. For destroyed SBs, the figure shows whether they'll be destroyed in the convective zone or below it, according to the analytical destruction estimates given by Equations 2 and 3. This figure assumes SBs are engulfed at their present-day orbital separations, and that all SBs orbit $1M_{\odot}$ stars (the average stellar mass reported for these SBs' planetary systems is $1.12M_{\odot}$, with a standard deviation of $\sim 17\%$).

Envelope ejection as defined here does not necessarily result in the formation of a stellar remnant in a close orbit with an SB because the SB must eject material deeper in the star in order to clear its orbit around the remnant. This process depends on the energy distribution mechanisms within the envelope, particularly in regions closer to the core than the SB's orbital separation during inspiral. Modeling this process

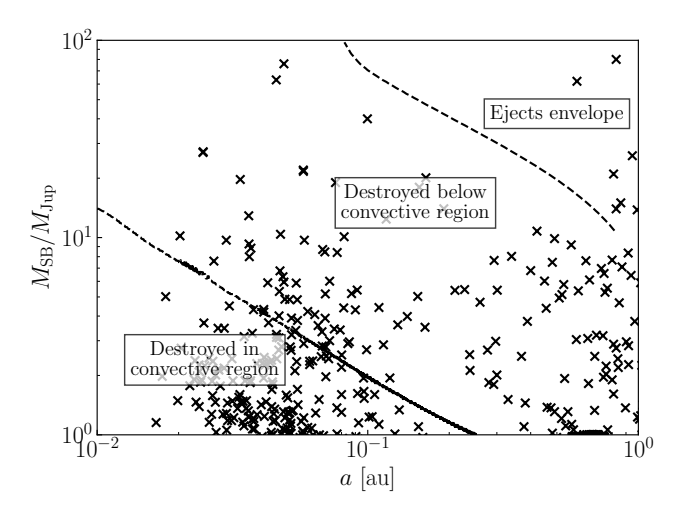


Figure 11. Engulfment outcomes for known substellar bodies (SBs, NASA Exoplanet Archive 2022), as a function of SB mass and orbital separation. This figure assumes that SBs are engulfed at their current separations and that they all orbit $1M_{\odot}$ stars. At a fixed SB mass, envelope ejection becomes easier as the star ascends the red giant branch because its binding energy decreases. A large fraction of SBs engulfed early in post-main-sequence evolution will dissolve in the convective region, yielding potential surface abundance enhancements of the 7 Li isotope. Envelope ejection does not necessarily result in the formation of a stellar remnant with a closely orbiting SB, since the SB must eject some material depper in the star in order to be in a stable orbit around the remnant. This process depends on how energy is distributed within the envelope, which we do not model here.

requires a detailed time-dependent treatment of the internal structure and energy transport mechanisms of the star throughout engulfment, which is outside of the scope of this work.

Under these assumptions, Figure 11 shows that massive SBs can eject the envelopes of evolved stars. The energy deposition predicted from the work done by the drag forces is larger in amplitude than the change in orbital energy during inspiral, yielding a lower minimum mass for envelope ejection compared to Figure 4. This difference is a result of the change in the mass enclosed by the orbit of the SB (Yarza et al. 2022b, in prep). This figure also shows that a substantial fraction of known SBs might be destroyed in the convective region of their host stars, particularly those at closer orbital separations because they are engulfed when the star is more compact and therefore disrupts them more easily. The ⁷Li contained in these SBs could be carried via convection to the surface, resulting in enhanced surface abundances.

6. CONCLUSIONS

We studied the engulfment of substellar bodies (SBs) by evolved stars using analytical and numerical techniques. Analytically, using the α formalism, we estimated that no SBs with masses $\lesssim 100 M_{\rm Jup}$ can eject the envelope of a Sun-like star before it evolves to $\approx 10 R_{\odot}$. In contrast, SBs as small as

 $\approx 10 M_{\rm Jup}$ can eject the envelope of a Sun-like star at the tip of the red giant branch (RGB).

We adapted the wind tunnel numerical framework, which has been extensively used to study interactions between evolved stars and compact objects, to interactions between evolved stars and SBs. We used this framework to perform hydrodynamical simulations of the flow in the vicinity of the engulfed SB, which enabled us to understand the morphology of the flow and to quantitatively determine the forces acting on the object. In turn, we used these forces to integrate the trajectory of the object inside the envelope. The numerical framework we introduced here can be used to study the dynamics of planetary engulfment using inexpensive simulations (compared to global simulations of engulfment) while accurately capturing the physics of the local flow.

We found that the inspiral of a substellar object between one and one hundred Jupiter masses can increase the luminosity of the star by up to several orders of magnitude for between one and a few thousand years, depending on the mass of the engulfed object and the evolutionary stage of the star.

Future work could explore the effect of engulfment on stellar structure, which will be significant at least for the most massive SBs, which could eject the envelope. Self-consistent modeling of the stellar structure during engulfment will also constrain observational signatures, such as the additional luminosity.

Similarly, the evolution of the internal structure of the SB remains a significant uncertainty in our calculations because it determines how far into the envelope it can survive, and consequently whether envelope ejection is possible. If the SB cannot survive, the changes in its internal structure will determine where its material is deposited within the star. Future work could perform local simulations of the internal structure of the SB subject to an external gravitational field, drag forces, and heat conduction to determine the stellar envelope conditions in which it will be destroyed, and the associated timescales.

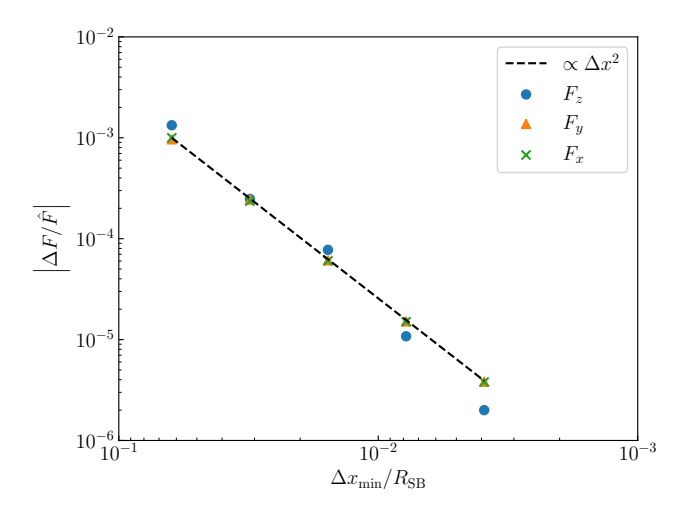


Figure 12. Relative error (compared to finest resolution simulation) in ram pressure and gravitational drag forces as a function of the minimum cell size Δx_{\min} .

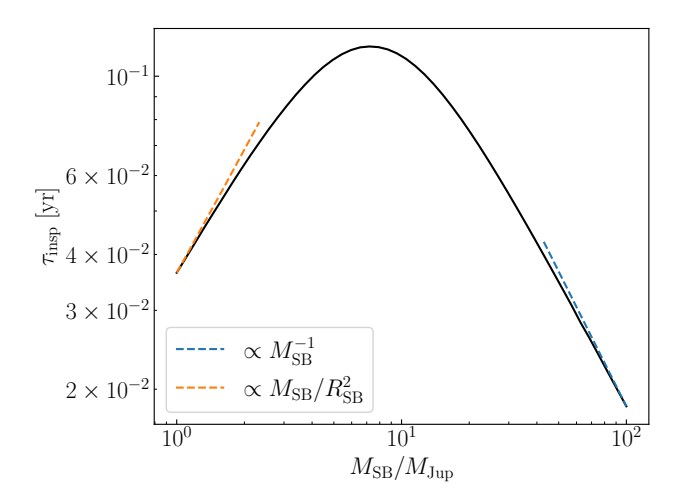


Figure 13. Inspiral time for substellar bodies as a function of their mass, inside a model of a $1M_{\odot}$ star evolved to $10R_{\odot}$.

We thank Brant Robertson and Yufeng Du for useful discussions. We acknowledge use of the lux supercomputer at UC Santa Cruz, funded by NSF MRI grant AST 1828315. We thank Brant Robertson and Josh Sonstroem for help using lux. The FLASH code was in part developed by the DOE NNSA-ASC OASCR Flash Center at the University of Chicago. R.Y. acknowledges support from a UCMEXUS-CONACYT Doctoral Fellowship. R.W.E. is supported by the National Science Foundation Graduate Research Fellowship Program (Award #1339067), the Heising-Simons Foundation, and the Vera Rubin Presidential Chair for Diversity at UCSC. A.M-B is supported by NASA through the NASA Hubble Fellowship grant HST-HF2-51487.001-A awarded by the Space Telescope Science Institute, which is operated by the Association of Universities for Research in Astronomy, Inc., for NASA, under contract NAS5-26555. E. R-R thanks the Heising-Simons Foundation and the NSF (AST-1911206, AST-1852393, and AST-1615881) for support. M.M. acknowledges support from the National Science Foundation under Grant No. 1909203. Any opinions, findings, and conclusions or recommendations expressed in this material are those of the authors and do not necessarily reflect the views of the NSF.

Software: FLASH 4.6.2 (Fryxell et al. 2000; Dubey et al. 2014, 2015), GNU Scientific Library 2.7 (Galassi et al. 2009), matplotlib 3.5.1 (Hunter 2007), MESA (Buchler & Yueh 1976; Fuller et al. 1985; Iglesias & Rogers 1993; Oda et al. 1994; Saumon et al. 1995; Iglesias & Rogers 1996; Itoh et al. 1996; Langanke & Martínez-Pinedo 2000; Timmes & Swesty 2000; Rogers & Nayfonov 2002; Irwin 2004; Ferguson et al. 2005; Cassisi et al. 2007; Chugunov et al. 2007; Cyburt et al. 2010; Potekhin & Chabrier 2010; Paxton et al. 2011, 2013, 2015, 2018, 2019), MESA SDK (Townsend 2019), numpy 1.21.4 (Harris et al. 2020), py_mesa_reader (Wolf & Schwab 2017), scipy 1.7.2 (Virtanen et al. 2020), yt 4.0.1 (Turk et al. 2011).

APPENDIX

A. NUMERICAL TESTS

A.1. Wind tunnel

We measured the ram pressure and gravitational drag forces in a simulation with $\varepsilon_{\rho}=0.4$ and $R_{\rm SB}/R_a=0.7$, as a function of resolution. Figure 12 shows the relative error in each component of both forces as a function of resolution when compared to our finest resolution simulation.

A.2. Inspiral integrator

We integrated the trajectory of an SB around a $1M_{\odot}$ point particle for a circular orbit and an orbit with eccentricity of 0.9. The initial separation was $9R_{\odot}$. We verified that the

energy and the radial and angular coordinates had relative errors smaller than 10^{-10} after 10^4 orbits in both cases.

We integrated inspirals inside a $1M_{\odot}$ star evolved to $10R_{\odot}$ for several SB masses. Figure 13 confirms that in the low and high mass limits the inspiral time scales as $M_{\rm SB}/R_{\rm SB}^2$ and $M_{\rm SB}^{-1}$, respectively (see equations 15 and 16). In this test, we used the analytical values for the drag coefficients.

B. DATA AND SOFTWARE AVAILABILITY

The software and data required to reproduce the results of this paper are available under the digital object identifiers

10.5281/zenodo.6368227 and 10.5281/zenodo.6371752, respectively.

REFERENCES

- Adamów, M., Niedzielski, A., Villaver, E., et al. 2015, A&A, 581, A94, doi: 10.1051/0004-6361/201526582
- Adamów, M., Niedzielski, A., Villaver, E., Wolszczan, A., & Nowak, G. 2014, A&A, 569, A55, doi: 10.1051/0004-6361/201423400
- Aguilera-Gómez, C., Chanamé, J., Pinsonneault, M. H., & Carlberg,
 J. K. 2016a, ApJL, 833, L24, doi: 10.3847/2041-8213/833/2/L24
 —. 2016b, ApJ, 829, 127, doi: 10.3847/0004-637X/829/2/127
- Almeida, L. A., Damineli, A., Rodrigues, C. V., Pereira, M. G., & Jablonski, F. 2017, MNRAS, 472, 3093, doi: 10.1093/mnras/stx2150
- Balachandran, S. C., Fekel, F. C., Henry, G. W., & Uitenbroek, H. 2000, ApJ, 542, 978, doi: 10.1086/317055
- Baumann, P., Ramírez, I., Meléndez, J., Asplund, M., & Lind, K. 2010, A&A, 519, A87, doi: 10.1051/0004-6361/201015137
- Beuermann, K., Dreizler, S., Hessman, F. V., et al. 2013, A&A, 558, A96, doi: 10.1051/0004-6361/201322241
- Bodenheimer, P. 1965, ApJ, 142, 451, doi: 10.1086/148310
- Bondi, H. 1952, MNRAS, 112, 195, doi: 10.1093/mnras/112.2.195
- Bondi, H., & Hoyle, F. 1944, MNRAS, 104, 273,
 - doi: 10.1093/mnras/104.5.273
- Breedt, E., Gänsicke, B. T., Girven, J., et al. 2012, MNRAS, 423, 1437, doi: 10.1111/j.1365-2966.2012.20965.x
- Brown, J. A., Sneden, C., Lambert, D. L., & Dutchover, Edward, J. 1989, ApJS, 71, 293, doi: 10.1086/191375
- Buchler, J. R., & Yueh, W. R. 1976, ApJ, 210, 440, doi: 10.1086/154847
- Cameron, A. G. W., & Fowler, W. A. 1971, ApJ, 164, 111, doi: 10.1086/150821
- Carlberg, J. K., Smith, V. V., Cunha, K., Majewski, S. R., & Rood, R. T. 2010, ApJL, 723, L103, doi: 10.1088/2041-8205/723/1/L103
- Carlos, M., Nissen, P. E., & Meléndez, J. 2016, A&A, 587, A100, doi: 10.1051/0004-6361/201527478
- Carlos, M., Meléndez, J., Spina, L., et al. 2019, MNRAS, 485, 4052, doi: 10.1093/mnras/stz681
- Casewell, S. L., Burleigh, M. R., Wynn, G. A., et al. 2012, ApJL, 759, L34, doi: 10.1088/2041-8205/759/2/L34
- Casewell, S. L., Belardi, C., Parsons, S. G., et al. 2020, MNRAS, 497, 3571, doi: 10.1093/mnras/staa1608
- Cassisi, S., Potekhin, A. Y., Pietrinferni, A., Catelan, M., & Salaris, M. 2007, ApJ, 661, 1094, doi: 10.1086/516819
- Chabrier, G., Baraffe, I., Leconte, J., Gallardo, J., & Barman, T. 2009, in American Institute of Physics Conference Series, Vol. 1094, 15th Cambridge Workshop on Cool Stars, Stellar Systems, and the Sun, ed. E. Stempels, 102–111, doi: 10.1063/1.3099078

- Charbonnel, C., & Balachandran, S. C. 2000, A&A, 359, 563. https://arxiv.org/abs/astro-ph/0005280
- Charbonnel, C., & Lagarde, N. 2010, A&A, 522, A10, doi: 10.1051/0004-6361/201014432
- Charpinet, S., Fontaine, G., Brassard, P., et al. 2011, Nature, 480, 496, doi: 10.1038/nature10631
- Chugunov, A. I., Dewitt, H. E., & Yakovlev, D. G. 2007, PhRvD, 76, 025028, doi: 10.1103/PhysRevD.76.025028
- Cyburt, R. H., Amthor, A. M., Ferguson, R., et al. 2010, ApJS, 189, 240, doi: 10.1088/0067-0049/189/1/240
- De, S., MacLeod, M., Everson, R. W., et al. 2020, ApJ, 897, 130, doi: 10.3847/1538-4357/ab9ac6
- Deepak, & Reddy, B. E. 2019, MNRAS, 484, 2000, doi: 10.1093/mnras/stz128
- Deliyannis, C. P., Cunha, K., King, J. R., & Boesgaard, A. M. 2000, AJ, 119, 2437, doi: 10.1086/301327
- Dubey, A., Antypas, K., Calder, A. C., et al. 2014, International Journal of High Performance Computing Applications, 28, 225, doi: http://dx.doi.org/10.1177/1094342013505656
- Dubey, A., Weide, K., Lee, D., et al. 2015, Software: Practice and Experience, 45, 233
- Everson, R. W., MacLeod, M., De, S., Macias, P., & Ramirez-Ruiz, E. 2020, ApJ, 899, 77, doi: 10.3847/1538-4357/aba75c
- Fabrycky, D., & Tremaine, S. 2007, ApJ, 669, 1298, doi: 10.1086/521702
- Ferguson, J. W., Alexander, D. R., Allard, F., et al. 2005, ApJ, 623, 585, doi: 10.1086/428642
- Fragos, T., Andrews, J. J., Ramirez-Ruiz, E., et al. 2019, ApJL, 883, L45, doi: 10.3847/2041-8213/ab40d1
- Fryxell, B., Olson, K., Ricker, P., et al. 2000, ApJS, 131, 273, doi: 10.1086/317361
- Fuller, G. M., Fowler, W. A., & Newman, M. J. 1985, ApJ, 293, 1, doi: 10.1086/163208
- Galassi, M., et al. 2009, GNU Scientific Library Reference Manual, 3rd edn.
- Gao, Q., Shi, J.-R., Yan, H.-L., et al. 2019, ApJS, 245, 33, doi: 10.3847/1538-4365/ab505c
- Geier, S., Edelmann, H., Heber, U., & Morales-Rueda, L. 2009, ApJL, 702, L96, doi: 10.1088/0004-637X/702/1/L96
- Grunblatt, S. K., Huber, D., Gaidos, E., et al. 2018, ApJL, 861, L5, doi: 10.3847/2041-8213/aacc67
- Grunblatt, S. K., Saunders, N., Sun, M., et al. 2022, arXiv e-prints, arXiv:2201.04140. https://arxiv.org/abs/2201.04140
- Gruzinov, A., Levin, Y., & Matzner, C. D. 2020, MNRAS, 492, 2755, doi: 10.1093/mnras/staa013

- Guidarelli, G., Nordhaus, J., Chamandy, L., et al. 2019, MNRAS, 490, 1179, doi: 10.1093/mnras/stz2641
- Harris, C. R., Millman, K. J., van der Walt, S. J., et al. 2020, Nature, 585, 357–362, doi: 10.1038/s41586-020-2649-2
- Hoyle, F., & Lyttleton, R. A. 1939, Proceedings of the Cambridge Philosophical Society, 35, 405, doi: 10.1017/S0305004100021150
- Hunter, J. D. 2007, Computing in Science & Engineering, 9, 90, doi: 10.1109/MCSE.2007.55
- Iglesias, C. A., & Rogers, F. J. 1993, ApJ, 412, 752, doi: 10.1086/172958
- -.. 1996, ApJ, 464, 943, doi: 10.1086/177381
- Irwin, A. W. 2004, The FreeEOS Code for Calculating the Equation of State for Stellar Interiors. http://freeeos.sourceforge.net/
- Itoh, N., Hayashi, H., Nishikawa, A., & Kohyama, Y. 1996, ApJS, 102, 411, doi: 10.1086/192264
- Jia, S., & Spruit, H. C. 2018, ApJ, 864, 169, doi: 10.3847/1538-4357/aad77c
- Kaaz, N., Murguia-Berthier, A., Chatterjee, K., Liska, M., & Tchekhovskoy, A. 2022, arXiv e-prints, arXiv:2201.11753. https://arxiv.org/abs/2201.11753
- Katz, B., Dong, S., & Malhotra, R. 2011, PhRvL, 107, 181101, doi: 10.1103/PhysRevLett.107.181101
- Kozai, Y. 1962, AJ, 67, 591, doi: 10.1086/108790
- Kruckow, M. U., Neunteufel, P. G., Di Stefano, R., Gao, Y., & Kobayashi, C. 2021, arXiv e-prints, arXiv:2107.05221. https://arxiv.org/abs/2107.05221
- Kumar, Y. B., Reddy, B. E., & Lambert, D. L. 2011, ApJL, 730, L12, doi: 10.1088/2041-8205/730/1/L12
- Langanke, K., & Martínez-Pinedo, G. 2000, Nuclear Physics A, 673, 481, doi: 10.1016/S0375-9474(00)00131-7
- Lee, D. 2013, Journal of Computational Physics, 243, 269, doi: https://doi.org/10.1016/j.jcp.2013.02.049
- Li, H., Aoki, W., Matsuno, T., et al. 2018, ApJL, 852, L31, doi: 10.3847/2041-8213/aaa438
- Li, X., Chang, P., Levin, Y., Matzner, C. D., & Armitage, P. J. 2020, MNRAS, 494, 2327, doi: 10.1093/mnras/staa900
- Littlefair, S. P., Dhillon, V. S., Marsh, T. R., et al. 2007, MNRAS, 381, 827, doi: 10.1111/j.1365-2966.2007.12285.x
- —. 2008, MNRAS, 388, 1582, doi: 10.1111/j.1365-2966.2008.13539.x
- -.. 2006, Science, 314, 1578, doi: 10.1126/science.1133333
- Liu, C., Li, L., Zhang, F., et al. 2012, MNRAS, 424, 1841, doi: 10.1111/j.1365-2966.2012.21285.x
- Livio, M., & Soker, N. 1984, MNRAS, 208, 763, doi: 10.1093/mnras/208.4.763
- MacLeod, M., Antoni, A., Murguia-Berthier, A., Macias, P., & Ramirez-Ruiz, E. 2017, ApJ, 838, 56, doi: 10.3847/1538-4357/aa6117
- MacLeod, M., Cantiello, M., & Soares-Furtado, M. 2018, ApJL, 853, L1, doi: 10.3847/2041-8213/aaa5fa

- MacLeod, M., & Loeb, A. 2020, ApJ, 895, 29, doi: 10.3847/1538-4357/ab89b6
- MacLeod, M., & Ramirez-Ruiz, E. 2015a, ApJL, 798, L19, doi: 10.1088/2041-8205/798/1/L19
- —. 2015b, ApJ, 803, 41, doi: 10.1088/0004-637X/803/1/41
- Mallick, A., Reddy, B. E., & Muthumariappan, C. 2022, arXiv e-prints, arXiv:2201.09643. https://arxiv.org/abs/2201.09643
- Martell, S. L., & Shetrone, M. D. 2013, MNRAS, 430, 611, doi: 10.1093/mnras/sts661
- Masset, F. S. 2017, MNRAS, 472, 4204, doi: 10.1093/mnras/stx2271
- Masset, F. S., & Velasco Romero, D. A. 2017, MNRAS, 465, 3175, doi: 10.1093/mnras/stw3008
- Maxted, P. F. L., Napiwotzki, R., Dobbie, P. D., & Burleigh, M. R. 2006, Nature, 442, 543, doi: 10.1038/nature04987
- McAllister, M. J., Littlefair, S. P., Baraffe, I., et al. 2015, MNRAS, 451, 114, doi: 10.1093/mnras/stv956
- Meléndez, J., Schirbel, L., Monroe, T. R., et al. 2014, A&A, 567, L3, doi: 10.1051/0004-6361/201424172
- Metzger, B. D., Giannios, D., & Spiegel, D. S. 2012, MNRAS, 425, 2778, doi: 10.1111/j.1365-2966.2012.21444.x
- Metzger, B. D., Shen, K. J., & Stone, N. 2017, MNRAS, 468, 4399, doi: 10.1093/mnras/stx823
- Monroe, T. R., Meléndez, J., Ramírez, I., et al. 2013, ApJL, 774, L32, doi: 10.1088/2041-8205/774/2/L32
- Murguia-Berthier, A., MacLeod, M., Ramirez-Ruiz, E., Antoni, A., & Macias, P. 2017, ApJ, 845, 173, doi: 10.3847/1538-4357/aa8140
- Mustill, A. J., & Villaver, E. 2012, ApJ, 761, 121, doi: 10.1088/0004-637X/761/2/121
- Naoz, S., Farr, W. M., & Rasio, F. A. 2012, ApJL, 754, L36, doi: 10.1088/2041-8205/754/2/L36
- NASA Exoplanet Archive. 2022, Planetary Systems Composite Parameters, Version: YYYY-MM-DD HH:MM, NExScI-Caltech/IPAC, doi: 10.26133/NEA13
- Nelemans, G., & Tauris, T. M. 1998, A&A, 335, L85. https://arxiv.org/abs/astro-ph/9806011
- Nordhaus, J., & Spiegel, D. S. 2013, MNRAS, 432, 500, doi: 10.1093/mnras/stt569
- Nordhaus, J., Wellons, S., Spiegel, D. S., Metzger, B. D., & Blackman, E. G. 2011, Proceedings of the National Academy of Sciences, 108, 3135, doi: 10.1073/pnas.1015005108
- Oda, T., Hino, M., Muto, K., Takahara, M., & Sato, K. 1994, Atomic Data and Nuclear Data Tables, 56, 231, doi: 10.1006/adnd.1994.1007
- Ostriker, E. C. 1999, ApJ, 513, 252, doi: 10.1086/306858
- Paczynski, B. 1976, in Structure and Evolution of Close Binary Systems, ed. P. Eggleton, S. Mitton, & J. Whelan, Vol. 73, 75

- Pala, A. F., Schmidtobreick, L., Tappert, C., Gänsicke, B. T., & Mehner, A. 2018, MNRAS, 481, 2523, doi: 10.1093/mnras/sty2434
- Parsons, S. G., Hermes, J. J., Marsh, T. R., et al. 2017, MNRAS, 471, 976, doi: 10.1093/mnras/stx1610
- Paxton, B., Bildsten, L., Dotter, A., et al. 2011, ApJS, 192, 3, doi: 10.1088/0067-0049/192/1/3
- Paxton, B., Cantiello, M., Arras, P., et al. 2013, ApJS, 208, 4, doi: 10.1088/0067-0049/208/1/4
- Paxton, B., Marchant, P., Schwab, J., et al. 2015, ApJS, 220, 15, doi: 10.1088/0067-0049/220/1/15
- Paxton, B., Schwab, J., Bauer, E. B., et al. 2018, ApJS, 234, 34, doi: 10.3847/1538-4365/aaa5a8
- Paxton, B., Smolec, R., Schwab, J., et al. 2019, ApJS, 243, 10, doi: 10.3847/1538-4365/ab2241
- Peterson, R. C., Tarbell, T. D., & Carney, B. W. 1983, ApJ, 265, 972, doi: 10.1086/160739
- Piau, L., & Turck-Chièze, S. 2002, ApJ, 566, 419, doi: 10.1086/324277
- Potekhin, A. Y., & Chabrier, G. 2010, Contributions to Plasma Physics, 50, 82, doi: 10.1002/ctpp.201010017
- Privitera, G., Meynet, G., Eggenberger, P., et al. 2016a, A&A, 593, A128, doi: 10.1051/0004-6361/201628758
- —. 2016b, A&A, 591, A45, doi: 10.1051/0004-6361/201528044
- Prša, A., Harmanec, P., Torres, G., et al. 2016, AJ, 152, 41, doi: 10.3847/0004-6256/152/2/41
- Qureshi, A., Naoz, S., & Shkolnik, E. L. 2018, ApJ, 864, 65, doi: 10.3847/1538-4357/aad562
- Rebassa-Mansergas, A., Zorotovic, M., Schreiber, M. R., et al. 2012, MNRAS, 423, 320, doi: 10.1111/j.1365-2966.2012.20880.x
- Reddy, B. E., & Lambert, D. L. 2005, AJ, 129, 2831, doi: 10.1086/430190
- Rogers, F. J., & Nayfonov, A. 2002, ApJ, 576, 1064, doi: 10.1086/341894
- Ruffert, M., & Arnett, D. 1994, ApJ, 427, 351, doi: 10.1086/174145
 Sandquist, E., Taam, R. E., Lin, D. N. C., & Burkert, A. 1998, ApJL, 506, L65, doi: 10.1086/311633
- Sandquist, E. L., Dokter, J. J., Lin, D. N. C., & Mardling, R. A. 2002, ApJ, 572, 1012, doi: 10.1086/340452
- Saumon, D., Chabrier, G., & van Horn, H. M. 1995, ApJS, 99, 713, doi: 10.1086/192204
- Schaffenroth, V., Barlow, B. N., Drechsel, H., & Dunlap, B. H. 2015, A&A, 576, A123, doi: 10.1051/0004-6361/201525701
- Schaffenroth, V., Casewell, S. L., Schneider, D., et al. 2021, MNRAS, 501, 3847, doi: 10.1093/mnras/staa3661
- Schlaufman, K. C., & Winn, J. N. 2013, ApJ, 772, 143, doi: 10.1088/0004-637X/772/2/143
- Schmidt, G. D., Szkody, P., Silvestri, N. M., et al. 2005, ApJL, 630, L173, doi: 10.1086/491702

- Shappee, B. J., & Thompson, T. A. 2013, ApJ, 766, 64, doi: 10.1088/0004-637X/766/1/64
- Siess, L., & Livio, M. 1999, MNRAS, 308, 1133, doi: 10.1046/j.1365-8711.1999.02784.x
- Silvestri, N. M., Lemagie, M. P., Hawley, S. L., et al. 2007, AJ, 134, 741, doi: 10.1086/519242
- Singh, R., Reddy, B. E., Bharat Kumar, Y., & Antia, H. M. 2019, ApJL, 878, L21, doi: 10.3847/2041-8213/ab2599
- Soares-Furtado, M., Cantiello, M., MacLeod, M., & Ness, M. K. 2020, arXiv e-prints, arXiv:2002.05275. https://arxiv.org/abs/2002.05275
- Socrates, A., Katz, B., Dong, S., & Tremaine, S. 2012, ApJ, 750, 106, doi: 10.1088/0004-637X/750/2/106
- Soker, N. 1998, AJ, 116, 1308, doi: 10.1086/300503
- Staff, J. E., De Marco, O., Wood, P., Galaviz, P., & Passy, J.-C. 2016, MNRAS, 458, 832, doi: 10.1093/mnras/stw331
- Steele, P. R., Saglia, R. P., Burleigh, M. R., et al. 2013, MNRAS, 429, 3492, doi: 10.1093/mnras/sts620
- Steffen, M. 1990, A&A, 239, 443
- Stephan, A. P., Naoz, S., Gaudi, B. S., & Salas, J. M. 2020, ApJ, 889, 45, doi: 10.3847/1538-4357/ab5b00
- Sun, M., Arras, P., Weinberg, N. N., Troup, N. W., & Majewski, S. R. 2018, MNRAS, 481, 4077, doi: 10.1093/mnras/sty2464
- Thun, D., Kuiper, R., Schmidt, F., & Kley, W. 2016, A&A, 589, A10, doi: 10.1051/0004-6361/201527629
- Tiesinga, E., Mohr, P. J., Newell, D. B., & Taylor, B. N. 2021, Rev. Mod. Phys., 93, 025010, doi: 10.1103/RevModPhys.93.025010
- Timmes, F. X., & Swesty, F. D. 2000, ApJS, 126, 501, doi: 10.1086/313304
- Townsend, R. 2019, MESA SDK for Linux, 20190503, Zenodo, doi: 10.5281/zenodo.2669541
- Turk, M. J., Smith, B. D., Oishi, J. S., et al. 2011, ApJS, 192, 9, doi: 10.1088/0067-0049/192/1/9
- van Roestel, J., Kupfer, T., Bell, K. J., et al. 2021, ApJL, 919, L26, doi: 10.3847/2041-8213/ac22b7
- Vanderburg, A., Rappaport, S. A., Xu, S., et al. 2020, Nature, 585, 363, doi: 10.1038/s41586-020-2713-y
- Villaver, E., & Livio, M. 2007, ApJ, 661, 1192, doi: 10.1086/516746
 —. 2009, ApJL, 705, L81, doi: 10.1088/0004-637X/705/1/L81
- Villaver, E., Livio, M., Mustill, A. J., & Siess, L. 2014, ApJ, 794, 3, doi: 10.1088/0004-637X/794/1/3
- Virtanen, P., Gommers, R., Oliphant, T. E., et al. 2020, Nature Methods, 17, 261, doi: 10.1038/s41592-019-0686-2
- Wallerstein, G., & Sneden, C. 1982, ApJ, 255, 577, doi: 10.1086/159859
- Webbink, R. F. 1984, ApJ, 277, 355, doi: 10.1086/161701
- Wolf, B., & Schwab, J. 2017, wmwolf/py_mesa_reader: Interact with MESA Output, 0.3.0, Zenodo, doi: 10.5281/zenodo.826958
- Yamazaki, R., Hayasaki, K., & Loeb, A. 2017, MNRAS, 466, 1421, doi: 10.1093/mnras/stw3207

Yan, H.-L., Shi, J.-R., Zhou, Y.-T., et al. 2018, Nature Astronomy, 2,

790, doi: 10.1038/s41550-018-0544-7

Zhang, M., & Penev, K. 2014, ApJ, 787, 131, doi: 10.1088/0004-637X/787/2/131

 $Zhou,\,Y.,\,Yan,\,H.,\,Shi,\,J.,\,et\,al.\,\,2019,\,ApJ,\,877,\,104,$

doi: 10.3847/1538-4357/ab1b4b